

The Early Evolution of Massive Stars: Radio Recombination Line Spectra

Eric Keto

Harvard-Smithsonian Center for Astrophysics, 60 Garden St., Cambridge, MA 02138

and

Qizhou Zhang

Harvard-Smithsonian Center for Astrophysics, 60 Garden St., Cambridge, MA 02138

and

Stanley Kurtz

CRyA, Universidad Nacional Autónoma de México, Apdo. Postal 3-72, 58090 Morelia, Michoacán, Mexico

ABSTRACT

Velocity shifts and differential broadening of radio recombination lines are used to estimate the densities and velocities of the ionized gas in several hypercompact and ultracompact HII regions. These small HII regions are thought to be at their earliest evolutionary phase and associated with the youngest massive stars. The observations suggest that these HII regions are characterized by high densities, supersonic flows and steep density gradients, consistent with accretion and outflows that would be associated with the formation of massive stars.

Subject headings: stars: early type — stars: formation — ISM: HII regions

1. Introduction

Massive star forming regions are marked by small (≤ 0.1 pc) HII regions (Gaume et al. 1995b; DePree et al. 1997; Tieftrunk et al. 1997; DePree et al. 1998; Wilson et al. 2003; DePree et al. 2000, 2004, 2005) that are characteristically different from many of the few

thousand ultracompact HII (UCHII) regions scattered throughout the galaxy (Wood & Churchwell 1989; Kurtz et al. 1994; Walsh et al. 1998; Giveon et al. 2005a,b). First, these very small HII regions have electron densities that are higher ($n_e \geq 10^5 \text{ cm}^{-3}$) than those of UCHII regions ($n_e \sim 10^4 \text{ cm}^{-3}$) (Kurtz 2000; Kurtz & Franco 2002; Pratap et al. 1992). It is unclear how high the densities might be, because the density cannot be reliably determined from the radio continuum if the gas is optically thick. Second, when observed at centimeter wavelengths, these small HII regions often show very broad radio recombination line (RRL) widths, more than 3 or 4 times the thermal line width (Altenhoff, Stritmatter & Wendker 1981; Zijlstra et al. 1990; Afflerbach et al. 1994; DePree et al. 1994; Gaume et al. 1995a; DePree et al. 1995, 1996, 1997; Keto et al. 1995; Johnson et al. 1998; Jaffe & Martín-Pintado 1999; Keto 2002a; Sewilo et al. 2004; Keto & Wood 2006). Not all the small HII regions have this property, but those that do are sometimes referred to as broad recombination line objects. The breadth of the RRLs could be caused by a combination of electron impact (pressure) broadening associated with high gas density plus broadening caused by spatially unresolved gas motions. However, the relative contributions of broadening due to gas pressure and gas motions are not known. Third, these HII regions often have continuum spectral energy distributions (SEDs) that are roughly linear with frequency over decades in wavelength from the centimeter to the submillimeter (Hofner et al. 1996; Franco et al. 2000; Testi et al. 2000; Beuther et al. 2004; Ignace & Churchwell 2004). The underlying cause of this scaling is not known although spatially unresolved density variations are a possibility.

These small and dense HII regions are sometimes referred to as hypercompact HII (HCHII) regions. While the term hypercompact implies a size smaller than ultracompact (UC), the three properties of high electron densities, broad recombination lines, and linear SEDs, are also seen in some UCHII regions ($\sim 0.1 \text{ pc}$). The common characteristic between these unusual UCHII regions and the HCHII regions might be that they are all young and at the earliest evolutionary stage, but the unusual UCHII regions might contain more or brighter stars than their smaller HCHII counterparts. The HCHII and unusual UCHII regions represent some of our best sources of information on the processes in the formation of massive stars, and this motivates our understanding of their special properties.

In this paper we report on multi-frequency RRL observations that address the origin of the three properties of the small HII regions and the processes of massive star formation. Because broadening due to pressure is dependent on frequency whereas broadening due to gas motions is independent of frequency, the widths of RRLs observed at more than one frequency can be used to separate the contributions of each broadening mechanism. Since the pressure broadening is proportional to the density, this separation allows a determination of the electron density. Similarly, since the broadening due to gas motions is proportional to the range of velocities, we can also measure the magnitude of the gas velocities.

2. Observations

We selected a few well-studied, very bright, very small HII regions that previous observations suggest have one or more of the three properties of the small HII regions. For each source we have one observation of the H30 α line made with the Submillimeter Array (SMA) and one or more observations of centimeter wavelength RRLs made with the National Radio Astronomy Observatory Very Large Array (VLA)¹

The SMA observations of the H30 α line (231.900959 GHz) in the HII regions G10.6-0.04, NGC7538-IRS1, W51e2, and G28.20-0.04 were made in 2005 September with a spectral resolution of 0.83 km s⁻¹, a bandwidth of 2 GHz, and an angular resolution of 1.0". Observations of G45.07+0.14 were made in 2005 October with an angular resolution of 0.4". The noise level obtained in each observation was 60 mJy beam⁻¹ channel⁻¹. Analysis of the data indicated that some of the baselines were not well-defined, hence the positions and flux densities of the sources are uncertain. The standard deviation of the flux of 3C454.4, measured once for each observation, is 39% of the average measured value (table 1). If we exclude the low measurement of 3C454.4 corresponding to the G45.07+0.14 data, then the standard deviation falls to 14% of the average. Our positions from the SMA agree with those of the VLA to better than the angular resolution. The HII regions are unresolved by the SMA observations, and hence the widths of their spectral lines are unaffected by baseline errors. The SMA data were processed in the SMA data reduction package MIR, and in MIRIAD.

Most of the VLA observations were made in 2003 and 2005. We reprocessed observations of the H76 α line in G45.07+0.14 (Garay et al. 1986) from the VLA archives. The observations of the H66 α line in G10.6-0.4 were previously reported in Keto (2002a). The other observations have not previously been published. Details of the observations are presented in table 2. The VLA data were processed in AIPS; calibration data are given in table 3. The recombination line spectra are shown in figures 1 to 5, and the line widths and velocities based are given in table 4.

3. Gas velocities, pressure broadening, and electron densities

Radio recombination lines in HII regions are broadened by three contributions: thermal broadening, dynamical broadening due to spatially unresolved motions in the HII region including both ordered flows and turbulence, and pressure broadening due to high electron

¹The National Radio Astronomy Observatory is a facility of the National Science Foundation operated under cooperative agreement by Associated Universities, Inc.

densities. We seek to estimate the separate contributions of each of the three broadening components by comparing the widths of RRL observed at different frequencies. This is possible because the width due to thermal and dynamical broadening, is independent of frequency while the width due to pressure broadening decreases with frequency as $\Delta\nu \sim \nu^{-4}$ (Brocklehurst & Seaton 1972; Griem 1974). Since the dynamical broadening is proportional to the gas velocity while the pressure broadening is proportional to gas density, from a pair of RRL observations we can estimate the velocities and densities in the ionized gas.

We determine the contributions of each of the three broadening mechanisms as follows. We assume that the dynamical broadening, $\Delta\nu_D$, and the thermal broadening, $\Delta\nu_T$, combine in quadrature,

$$\Delta\nu_G = \sqrt{\Delta\nu_D^2 + \Delta\nu_T^2}. \quad (1)$$

This width due to gas motions, both thermal and spatially unresolved ordered flows and turbulence, combines with the Lorentzian width, $\Delta\nu_L$, due to pressure broadening to produce a Voigt profile with width, $\Delta\nu_V$. We approximate the width of the Voigt profile by an algebraic expression (Olivero & Longbothum 1977; Gordon & Sorochenko 2002, equation 2.72),

$$\Delta\nu_V = 0.5343\Delta\nu_L + [\Delta\nu_G^2 + (0.4657\Delta\nu_L)^2]^{1/2} \quad (2)$$

where $\Delta\nu_V$ is the full-width at half-maximum (FWHM) of the Voigt profile, $\Delta\nu_L$ the FWHM of the Lorentzian, and $\Delta\nu_G$ the FWHM of the Gaussian. Because of the rapid decrease in pressure broadening with frequency, the width of an RRL at a high enough frequency must be due solely to thermal broadening and spatially unresolved gas motions. Therefore we assume that this broadening, $\Delta\nu_G$ in equation 2, is given by the observed width of our highest frequency RRL, H30 α . If we compare the width of the H30 α line to that of a lower frequency line, any increased width observed in the lower frequency line must be due to pressure broadening because the width $\Delta\nu_G$ is independent of frequency. We can then calculate the width due to pressure broadening, $\Delta\nu_L$, by solving the quadratic equation 2.

The range of gas velocities is estimated from equation (1). Assuming an ionized gas temperature of 8000 K, the dynamical widths are 15.3, 8.3, 27.1, 18.7 and 53.9 kms⁻¹ for G10.6-0.4, G28.20-0.04N, G45.07+0.14, W51e2, and NGC 7538-IRS1 respectively.

The electron density may be estimated from the ratio of $\Delta\nu_L$ and $\Delta\nu_T$. For α ($\Delta N = 1$) transitions, the ratio of the Lorentzian width, $\Delta\nu_L$, resulting from pressure broadening, and the thermal width, $\Delta\nu_T$, is given by (Keto et al. 1995),

$$\frac{\Delta\nu_L}{\Delta\nu_T} = 1.2 \left(\frac{n_e}{10^5} \right) \left(\frac{N}{92} \right)^7 \quad (3)$$

where n_e is the electron density in cm⁻³, and N is the principal quantum number.

As an example, we calculate the electron density in G10.6-0.4 from the H30 α and H92 α RRL observations as follows. We use the width of the H30 α line, 24.5 km s⁻¹ (table 4) to estimate $\Delta\nu_G$ at the frequency of the H92 α line. Thus $\Delta\nu_G = 0.678$ MHz. The measured width of the H92 α line is $\Delta\nu_V(\text{H92}\alpha) = 1.03$ MHz. With these values and equation 2, the estimate of the width due to pressure broadening is $\Delta\nu_L = 0.578$ MHz or 20.9 km s⁻¹. The thermal width, assuming a temperature of 8000 K, is $\Delta\nu_T = 1.43$ MHz or 19.1 km s⁻¹. The width due to gas motions is $\Delta\nu_D = \sqrt{24.5^2 - 19.1^2} = 15.3$ km s⁻¹. The electron density from equation 3 is 9.1×10^4 cm⁻³. Similarly, from the observations of the other centimeter RRLs observed in G10.6-0.4, the electron densities are 7.8×10^5 cm⁻³ from the H66 α line and 2.5×10^6 cm⁻³ from the H53 α line. Comparing these three RRL, the electron density increases with the RRL frequency. If there is a density gradient in G10.6-0.4 this would suggest that the higher frequency lines are seeing deeper into the nebula where the electron densities are higher.

3.1. Uncertainties

We can check our approximation of negligible pressure broadening in the H30 α line from 3. For the H30 α line, this ratio is less than one as long as the density is less than 3×10^8 cm⁻³. Thus our assumption of negligible pressure broadening in the H30 α line is valid up to this density.

The lines in our sample are not consistently Gaussians or by Lorentzian. One possibility is that the asymmetric line profiles indicate asymmetries in the gas motions in the HII regions, for example, ordered flows rather than isotropic turbulence. We determine the line widths by fitting Gaussians because this provides a reasonable estimate if the observed profiles differ from a Gaussian most strongly in the wings and are similar in the core where the width is measured. A comparison of the line widths derived by fitting Gaussians to Voigt profiles provides an informal estimate of the possible error introduced by this method. If the Voigt profile is composed of a Gaussian and a Lorentzian of equal FWHM, then a Gaussian fit overestimates the true FWHM of the Voigt by 10%.

We find that the procedure of using Gaussian line widths in equation 2 to estimate the pressure broadening is a more reliable method than some alternatives. For example, one could imagine fitting a Voigt profile directly to an observed low frequency line to determine simultaneously both the Gaussian and Lorentzian components. However, we find this unreliable because the fitting procedure assigns the line width to either the Gaussian or Lorentzian components primarily on the shape of the line wings where the profiles differ most strongly, but the signal-to-noise ratio is the weakest. Alternatively, one might estimate the FWHM

directly from the 3 channels with the peak and half-power emission. However, because this estimate relies on single channel measurements it is less reliable than a line-fitting procedure that uses measurements at all the channels across the line profile.

Several lines of evidence, discussed later in the paper suggest that there are density variations within the HII regions. Because all the HII regions in our sample are unresolved, the measured electron density represents the average within the HII region. The size of the HII region within the beam (filling factor) does not affect this estimate of the average density because the electron densities are determined from the line widths rather than the emission intensity. However, the unknown density structure of the HII region creates some uncertainty. If there are significant variations in optical depth with frequency then it is possible that lines at different frequencies could be generated in different locations within the HII region.

Aside from the systematic effects, the uncertainty in the average electron density is given by the standard propagation of errors, assuming the errors in the widths are independent. Uncertainties in the electron densities are listed in table 5 and for the line center velocities and widths in table 4.

3.2. Electron densities from the radio continuum

At the high densities in our HII regions, the centimeter continuum emission is optically thick to free-free emission. This can be determined from the formula (eqn. A.1b, Mezger & Henderson 1967) or (eqn. 10, Keto 2003),

$$\tau_\nu = 8.235 \times 10^{-2} \left(\frac{T_e}{\text{K}} \right)^{-1.35} \left(\frac{\nu}{\text{GHz}} \right)^{-2.1} \left(\frac{n_e^2 L}{\text{pc cm}^{-6}} \right) \quad (4)$$

where T_e is the electron temperature and $n_e^2 L$ is the electron density squared times the path length. For a characteristic size of 0.01 pc, an HII region has an optical depth of unity at 22 GHz (1.3 cm) if the electron density is $4 \times 10^5 \text{ cm}^{-3}$. This means that the formulae for optically thin emission (e.g. Mezger & Henderson 1967) are not useful for the HII regions in our sample, and probably not for small, high-density HII regions in general.

If the gas is optically thick to free-free emission, and the electron density is estimated from the radio continuum by incorrectly assuming optically thin emission, then the derived electron density is just that density required to make the optical depth unity. This can be understood by a simple example. The radio free-free emission through a slab of uniform gas density and temperature is,

$$S_\nu = 2kT_e(\nu^2/c^2)[1 - e^{-\tau_\nu}](\text{Jy/Sr}) \quad (5)$$

The optically thin approximation amounts to replacing $[1 - \exp(-\tau_\nu)]$ by τ_ν so that,

$$S_\nu \approx 2kT_e(\nu^2/c^2)\tau_\nu \quad (6)$$

whereas, in the optically thick limit,

$$S_\nu \approx 2kT_e(\nu^2/c^2) \quad (7)$$

Thus if the HII region is optically thick (equation 7) but τ_ν is derived assuming equation 6, then the derived value of the optical depth is 1, and the electron density derived from equation 4 is the density required to make $\tau_\nu = 1$. Thus at 22 GHz (1.3 cm), the electron density derived for an HII region with a size of 0.01 pc is never be greater than about 10^5 cm^{-3} if the optically thin formulae are used – regardless of the true density. This underestimate also affects quantities derived from the electron density such as the number of ionizing photons required to balance recombinations which in turn is often used to derive the spectral types of the exciting stars.

Formulas for spherical HII regions that have a density gradient such that the central part of the HII region is optically thick are derived in Keto (2003). However, these formulae require a specification of the size of the optically thick region.

3.3. The correlation of line widths, velocities, and frequencies

As shown in table 4, the line widths decrease with increasing frequency in all cases. This suggests the increasing importance of pressure broadening at lower frequencies. For sources with more than one centimeter RRL observed, the electron densities increase with the increasing frequency of the centimeter line used in the analysis. The one exception is the electron density calculated from the H66 α line in NGC7538-IRS1. This line is very much wider and out of character with the other measurements in our sample. Aside from this one exception, the correlation of density with observing frequency indicates that the higher frequency lines are associated with higher density gas. The line center velocities also increase (redshift) with frequency, except for the lines of NGC7538-IRS1.

The combination of the two correlations, line center velocity with frequency and line width with frequency was first noticed in W3(OH) by Berulis & Ershov (1983). Welch & Marr (1987) and Keto et al. (1995) interpreted the dual correlation as evidence for an accelerating flow within a density gradient (Guilloteau et al. 1983). A full explanation is given in Keto et al. (1995) (see also Brocklehurst & Seaton (1972)) and can be summarized as follows: The peak intensity of RRLs is proportional to the density squared and inversely proportional

to the line width. Thus the peak intensity of optically thin high frequency lines with negligible pressure broadening is proportional to the density squared. The peak intensity of lower frequency lines is proportional to the first power of the density since the pressure broadened line width is itself proportional to density. Thus in spatially unresolved observations of gas with a density gradient, the higher frequency RRLs are dominated by emission from the higher density gas while the lower frequency RRLs include contributions from both high and low density gas. An observed difference in velocity between the high and low frequency lines thus indicates a difference in velocity between the high and low density gas.

The correlation of velocities and width with frequency therefore indicates that in these HII regions there is both a flow and a density gradient. The two are naturally related by the conservation of mass and the geometry of the flow. In general, if the flow is either outward and diverging or inward and converging then conservation of mass requires that there be a density gradient except in the unique circumstance that the variation of the flow speed exactly cancels the geometric divergence or convergence.

4. Continuum Spectral Indices

We determined the spectral energy distributions (SEDs) of the HII regions in our sample using our own millimeter and centimeter observations and data collected from the literature. We selected only those data with angular resolutions close to $1''$ specifically excluding single dish observations. Most of the data for NGC7538-IRS1 and G45.07+0.14 are from Pratap et al. (1992, table 1) and Garay et al. (1986, table 3), respectively. The rest of the observations are listed in table 6. Most of these data do not include estimated uncertainties. However, the calibration of radio data is fairly standard. Many of the reported observations were made at the VLA that typically calibrated flux densities to better than 20% at 1.3 cm at the dates of the observations and much better at longer wavelengths. As noted in §2, we estimated our SMA observations to be calibrated to better than 39%.

The spectral energy distributions are shown in figures 6 through 10. Along with each observed SED, shown as crosses, the figures show two model SEDs as solid lines. One model SED is based on a single HII region with a power-law density gradient. The continuum flux density for this model is calculated as in Keto (2003). The radio free-free emission of a spherical HII region seen as an unresolved source is,

$$S_\nu = 4\pi k T_e \nu^2 / c^2 \int_0^{\theta_0} \theta [1 - e^{-\tau_\nu}] d\theta \quad (8)$$

Here, θ is an angular coordinate on the plane of the sky, $\theta = \sqrt{x^2 + y^2}/D$ with coordinate

axes x and y are centered on the HII region, $\theta_0 = R_0/D$ where R_0 is the radius of the HII region, and D the distance to the source. An approximation to the free-free optical depth is, Mezger & Henderson (1967, equation A.1a),

$$\tau_\nu = 8.235 \times 10^{-2} \left(\frac{T_e}{\text{°K}} \right)^{-1.35} \left(\frac{\nu}{\text{GHz}} \right)^{-2.1} \left(\frac{EM}{\text{pc cm}^{-6}} \right) \quad (9)$$

where T_e is the electron temperature, and EM is the emission measure, $n_e^2 L$.

The model parameters for all sources are listed in table 7. The other model is an SED based on constant density HII regions. The figures for NGC7538-IRS1 and W51e2 show the SEDs from multi-component models suggested by Pratap et al. (1992) and Rudolph et al. (1990). These are both based on constant density HII regions plus dust. The dust emission enters as (Pratap et al. 1992, equation 1),

$$S_\nu(\text{Jy}) = 52.36 M_\odot \left(\frac{0.2}{\lambda_{mm}} \right)^{\beta+3} \left[\exp \left(\frac{14.4}{\lambda_{mm} T_d} \right) - 1 \right]^{-1} D_{kpc}^{-2} \quad (10)$$

where S_ν is the dust emission in Jy, M is the mass of the dusty gas in M_\odot , β is the spectral index of the dust emissivity, T_d is the dust temperature in Kelvin, and D is the distance in kpc.

The multi-component model for NGC7538-IRS1 (Pratap et al. 1992) nicely illustrates how a density gradient within an HII region can stretch the transition between optically thick and thin frequencies resulting in an SED with an intermediate spectral index. In this model there are two concentric spherical regions each of uniform but different densities. The smaller, higher density component produces an emission curve that is shifted upward and to the right of the curve for the larger, lower density component (figure 6). The emission from the two components combines to produce an SED of intermediate slope. An HII region with a continuous density gradient can be considered as the logical extension of this two component model to many nested smaller and denser HII regions. Lugo et al. (2004(@)) also model the NGC 7538-IRS1 HII region with a density gradient that they suggest is due to a wind off a photo-evaporating disk.

The SED modeling combined with the recombination line measurements shows that dust is not a significant contributor to the continuum emission measured at high angular resolution from these sources. (See also Kurtz (2005), DePree et al. (1998), and DePree et al. (2000).) Consider W51e2 as an example. As seen in figure 7, the HII region can be modeled with uniform, low-density ionized gas, with the 147 and 230 GHz emission arising from dust (Rudolph et al. 1990). Figure 7 shows that with this approach, the free-free continuum emission at 230 GHz would be about a factor of 10 below the observed emission. However, the line-to-continuum ratio should be approximately one at this frequency

(Gordon & Sorochenko 2002). Hence, if the free-free continuum were this low, the H30 α recombination line would also have a much lower flux density — so low that the line would not be detected in our observations. Stated another way, the recombination line emission cannot be 10 times greater than the free-free continuum emission at this frequency. Therefore, most of the continuum emission observed by the interferometer at 231.901 GHz must be free-free, hence the electron density must be higher, and a density gradient is required.

The high frequency emission observed in large beams (20 – 30'') around these bright HII regions certainly arises from dust. Again take W51e2 as an example. Jaffe et al. (1984) report a flux density of 1200 Jy beam⁻¹ at 750 GHz and 40'' angular resolution. We assume, as in the model of Rudolph et al. (1990), that this emission is from cool dust in the large-scale molecular cloud surrounding the HII region. Because the dust is cool (50 - 100 K), a large mass of dust is required (4500 M $_{\odot}$, Rudolph et al. (1990)) to produce the observed 750 GHz flux density. While the emission from this dust is also sufficient to produce the 90 and 230 GHz flux density that is observed by interferometers, the cool dust is not the source of this emission because it is not possible that this large mass of cool dusty gas is within the spatial scale defined by the arc second angular resolution of the interferometers. However, the ionized gas is sufficiently hot (10⁴ K) that only a small mass (0.01 M $_{\odot}$), consistent with the mass of the HII regions, is required to produce the 90 - 230 GHz flux density. Similar considerations apply to the multi-component models of other HII regions, for example, the model discussed earlier for NGC7538-IRS1 (Pratap et al. 1992).

On a spatial scale similar to that of HCHII and UCHII regions, continuum emission from dust has been observed by the SMA in the nearby (1.7 kpc) massive star forming region NGC6334 by Hunter et al. (2006). The dusty clumps of arcsecond scale in NGC6334 have continuum emission on the order of 1 Jy. Scaled to the distance of W51, the dust in such clumps would be a minor contributor (60 mJy) to the continuum emission. Thus, high angular resolution observations of dusty clumps in NGC6334 are consistent with the interpretation of negligible dust contribution to the emission observed at high angular resolution in more distant bright HII regions.

5. Discussion

The observations suggest that pressure broadening of the centimeter RRLs is important in small HII regions. This contradicts the interpretation of some previous studies. In particular, on the basis of electron densities calculated by assuming constant gas density and optically thin emission, Gaume et al. (1995a), DePree et al. (1997), and DePree et al. (2005) have suggested that the electron densities in NGC7538-IRS1, W49, and SgrB2 are

too low to cause significant pressure broadening in the $H66\alpha$ line. However, the RRL observations suggest that the electron density in NGC7538-IRS1 is two orders of magnitude greater than the 10^5 cm^{-3} derived by Gaume et al. (1995a) and sufficient to cause significant pressure broadening. Jaffe & Martín-Pintado (1999) report observations of millimeter RRL of several sources, including G10.6-0.4 and NGC7538-IRS1. They concluded that the RRL widths are not due to pressure broadening because the observed widths of different recombination lines do not scale as the fourth power of the frequency. Their conclusion was based on a comparison of observations with different angular resolutions. It has been demonstrated that low angular resolution observations may suffer confusion from more-extended, lower-density gas (Simpson 1973a,b; Gulyaev & Sorochenko 1974; Smirnov et al. 1984; Gordon & Sorochenko 2002). We concur with Gaume et al. (1995a); DePree et al. (1997, 2005); Jaffe & Martín-Pintado (1999) that broadening due to gas motions is a significant contribution to the observed line widths, but we find that pressure broadening is also significant, particularly for the lower frequency lines.

The intermediate SEDs of small HII regions imply a density gradient as would arise from a divergence or convergence in the flow of ionized gas in an HII region. Other interpretations are possible. Franco et al. (2000), Kurtz & Franco (2002) and Kim & Koo (2002) suggested that the various densities are due to the hierarchical structure of the molecular cloud prior to its ionization by a massive star. The intermediate SEDs can also be created by density variations other than gradients. Ignace & Churchwell (2004) suggested that an HII region is actually an ensemble of differently-sized clumps, each of uniform but different density. One problem with these models of pre-existing structure or clumps is that their survival time is approximately their sound crossing time. This timescale seems impossibly short if the high density clumps are substructures within an HCHII ($t_c \leq 1000$ yrs for $R < 0.01$ pc).

The interpretation of density gradients and resulting high electron densities in small HII regions also contradicts the interpretation of significant dust emission in a number of other studies. For example, Rudolph et al. (1990); Pratap et al. (1992); Testi et al. (2000); Schilke et al. (1990); Beuther et al. (2004, 2006) model the small HII regions, W51e2, NGC7538-IRS1, G9.62+0.19-F, and Orion-KL-SMA1 respectively, with low and constant density gas and assume that dust makes up the emission at high frequencies. Testi et al. (2000) also provide an alternative model with a stellar wind rather than dust to supply the high frequency emission. These models with low and constant density have difficulty in explaining the broad RRL line widths. If the density is low, then the widths must be due to dynamical broadening created by a supersonic flow. However, a constant density is not generally consistent with supersonic flows. In general, a strong density gradient is required to create the strong pressure gradient needed to drive the flow.

6. Conclusions

1. The radio recombination line widths increase with decreasing frequency in all cases. This indicates the greater importance of pressure broadening at lower frequencies.

2. The electron densities calculated by comparison of centimeter recombination lines with the H30 α millimeter line increase with increasing frequency of the centimeter line. This suggests that the higher frequency lines are generated in denser gas and suggest that density gradients exist in small HII regions.

3. Supersonic line widths are observed in the H30 α RRL. This line is at a frequency high enough that pressure broadening is negligible provided that the density of the emitting gas is less than 10^8 cm^{-3} . The large line widths suggest the presence of supersonic motions within the HII regions.

3. The electron densities in HCHII and UCHII regions are generally high enough that the gas is optically thick at centimeter wavelengths. This means that electron densities cannot be calculated from radio continuum observations using formulae that assume optically thin emission. Instead formulae appropriate for partially optically thick emission must be used.

4. At high frequencies ($\geq 100 \text{ GHz}$) and high angular resolution ($\sim 1''$) the observed continuum emission is mostly free-free emission and not from dust. Comparisons based on high frequency observations with different beam sizes can lead to erroneous conclusions. High frequency emission at low angular resolution ($\geq 10''$) is probably from dust, but associated with the large-scale, overlying molecular cloud.

S. Kurtz acknowledges support from UNAM, DGAPA project IN106107.

REFERENCES

- Afflerbach, A., Churchwell, E., Hofner, P., & Kurtz, S. 1994, *ApJ*, 437, 697
- Altenhoff, W.J., Stritmatter, P.A., & Wendker, H.J. 1981, *AA*, 93, 48
- Berulis, I.I. & Ershov, A.A., 1983, *Soviet Astr. Lett*, 9,341
- Beuther, H., Zhang, Q., Greenhill, L. J., Reid, M. J., Wilner, D., Keto, E., Marrone, D., Ho, P. T. P., Moran, J. M., Rao, R., Shinnaga, H., & Liu, S.-Y. 2004, *ApJ*, 616, L31
- Beuther, H., Zhang, Q., Reid, M. J., Hunter, T. R., Gurwell, M., Wilner, D., Zhao, J.-H., Shinnaga, H., Keto, E., Ho, P. T. P., Moran, J. M., & Liu, S.-Y. 2006, *ApJ*, 636, 323
- Brocklehurst, M., & Seaton, M.J. 1972, *MNRAS*, 157, 179
- Brown, R.L., Lockman, F.J., & Knapp, G.R., 1978, *ARAA*, 16, 445
- DePree, C.G., Goss, W.M., Palmer, P., & Rubin, R. 1994, *ApJ* 428, 670
- DePree, C.G., Gaume, R.A., Goss, W.M., & Claussen, M.J. 1995, *ApJ*, 451, 284
- DePree, C.G., Gaume, R.A., Goss, W.M., & Claussen, M.J. 1996, *ApJ*, 464,788
- DePree C.G., Mehringer, D.M.,& Goss, W.M. 1997, *ApJ*, 482, 307
- DePree, C.G., Goss, W.M., & Gaume, R.A. 1998, *ApJ*, 500, 847
- De Pree, C. G.; Wilner, D. J.; Goss, W. M.; Welch, W. J.; McGrath, E. 2000, *ApJ*, 540, 308
- De Pree, C.G., Wilner, D.J., Mercer, A.J., Davis, L.E., Goss, W.M., Kurtz, S. 2004, *ApJ*, 600, 286
- DePree, C.G., Wilner, D.J., Deblasio, J., Mercer, A.J., & Davis, L.E. 2005, *ApJ*, 624, L101
- Franco, J., Kurtz, S., Hofner, P., Testi, L., Guillermo, G.-S., & Martos, M. 2000, *ApJ*, 542, L143
- Garay, G., Reid, M.J., & Moran, J.M. 1985, *ApJ*, 289, 681
- Garay, G., Rodriguez, L.F., & van Gorkom, J.H. 1986, *ApJ*, 309, 553
- Gaume, R.A., Goss, W.M., Dickel, H.R., Wilson, T.L., & Johnston, K. 1995a, *ApJ*, 438, 776
- Gaume, R.A., Claussen, M.J., DePree, C.G., Goss, W.M., & Mehringer, D.M. 1995b, *ApJ*, 449, 663

- Giveon, U., Becker, R. H., Helfand, D. J., White, R. L., 2005, *AJ*, 129, 348
- Giveon, U., Becker, R. H., Helfand, D. J., White, R. L., 2005, *AJ*, 130, 156
- Gordon, M.A. & Sorochenko, P.N. 2002, *Radio Recombination Lines. Their Physics and Astronomical Applications*, (Dordrecht: Kluwer)
- Griem, H.R. 1974, *Spectral Line Broadening by Plasmas*, (New York: Academic)
- Guilloteau, S., Stier, M.T., & Downes, D., 1983, *AA*, 126, 10
- Gulyaev, S.A., & Sorochenko, R.L. 1974, *Astron. Zh.*, 51, 1237
- Ho, P., & Haschick, A.D. 1981, *ApJ*, 248, 622
- Hoang-Binh, D. 1972, *Mém. Roy. Soc. Liège* 3, 367
- Hofner, P., Kurtz, S., Churchwell, E., Walmsley, C. & Cesaroni, R. 1996, *ApJ*, 460, 359
- Hunter, T., Phillips, T.G., & Menten, K.M. 1997, *ApJ*, 478, 283
- Hunter, T.R., Brogan, C.L., Megeath, S.T., Menten, K.M., Beuther, H., & Thorwirth, S. 2006, *ApJ*, 649, 888
- Ignace, R., & Churchwell, E. 2004, *ApJ*, 610, 351
- Jaffe, D.T., Becklin, E.E., & Hildebrand, R.H. 1984, *ApJ*, 279, L51
- Jaffe, D.T., & Martín-Pintado, J. 1999, 520, 162
- Johnson, C.O., DePree, C.G., & Goss, W.M. 1998, *ApJ*, 500, 302
- Keto, E., Welch, W., Reid, M., & Ho, P.T.P. 1995, *ApJ*, 444, 765
- Keto, E. 2002a, *ApJ*, 568, 754
- Keto, E. 2002b, *ApJ*, 580, 980
- Keto, E. 2003, *ApJ*, 599, 1196
- Keto, E., & Wood, K. 2006, *ApJ*, 637, 850
- Keto, E. 2006, *ApJ*, submitted, astro-ph/0603856
- Kim, K.-T., & Koo, B.-C. 2002, *RevMexAA Ser. Conf.*, 12, 27
- Kurtz, S., Churchwell, E., & Wood, D. 1994, *ApJS*, 91, 659

- Kurtz, S.E., Watson, A.M., Hofner, P., Otte, Birgit, 1999, ApJ, 514, 232
- Kurtz, S. 2000, RevMexAA Ser. Conf., 9, 169
- Kurtz, S. 2005, in Proc. 227th Symp. IAU., *Massive Star Birth: A Crossroads of Astrophysics*, eds: Cesaroni, R., Felli, M., Churchwell, E., & Walmsley, M., Cambridge Univ. Press
- Kurtz, S., & Franco, J., 2002, RevMexAA Ser. Conf., 12, 16
- Lugo, J., Lizano, S., & Garay, G., 2004, ApJ, 614, 807
- Mehring, D. 1994, ApJS, 91, 713
- Mezger, P.G., & Henderson, A.P. 1967, ApJ, 147, 471
- Olivero, J.J. & Longbothum, R.L., 1977, JQSRT, 17 233
- Parker, E.N., 1958, ApJ, 128, 664
- Pratap, P., Snyder, L.E., & Batrla, W. 1992, ApJ, 387, 241
- Rudolph, A., Welch, W.J., Palmer, P., & Dubrulle, B. 1990, ApJ, 363, 528
- Sewilo, M., Churchwell, E., Kurtz, S., Goss, W.M., & Hofner, P. 2004, ApJ, 605, 285
- Schilke, P., Mauersberger, R., Walmsley, C.M., & Wilson, T.J. 1990, AA, 227, 220
- Simpson, J.P. 1973a, ApSS, 20, 187
- Simpson, J.P. 1973b, PASP, 85, 479
- Sollins, P., & Ho, P.T.P. 2005, ApJ, 630, 987
- Sollins, P., Zhang, Q., Keto, E., & Ho, P.T.P 2005b, ApJ, 631, 399
- Smirnov, G.T., Sorochenko, R.L., & Pankonin, V. 1984, AA, 135, 116
- Su, Y.-N., Liu, S.-Y., Lim, J., Ohashi, N., Beuther, H., Zhang, Q., Sollins, P., Hunter, T., Sridharan, T.K., & Zhao, J.-H. 2004, ApJ, 616, L39
- Testi, L., Hofner, P., Kurtz, S., & Rupen, M. 2000, AA, 359, L5
- Tieftrunk, A. R., Gaume, R. A., Claussen, M. J., Wilson, T. L., & Johnston, K. J. 1997, AA, 318, 931

- Turner, B.E., & Matthews, H.E. 1984, ApJ, 277, 164
- Ulrich, R. 1976, ApJ, 210, 377
- Walsh, A.J., Burton, M.G., Hyland, A.R., & Robinson, G. 1998, MNRAS, 301, 640
- Welch, Wm.J., & Marr, J., 1987, ApJL, 317, L21
- Wilson, T.L., Boboltz, D.A., Gaume, R.A., & Megeath, S.T., 2003, ApJ, 597, 434
- Wood, D.O.S., Wood, & Churchwell, E. 1989, ApJS, 69, 831
- Zhang, Q., Ho, P.T.P., & Ohashi, H. 1998, ApJ, 494, 636
- Zijlstra, A.A., Pottasch, S.R., Engels, D., Roelfsema, P.R., te Lintel Hekkert, P., & Umana, G. 1990, MNRAS, 246, 217

Table 1. Calibration of Millimeter Observations

Source	Band	Flux		Bandpass		Gain	
		Calibrator	Flux Jy	Calibrator	Flux Jy	Calibrator	Flux Jy
G10.60 -0.4	SMA	Ceres	0.7	3C454.3	16.8	PKS 1911-201	1.4
G28.20 - 0.04 N	SMA	3C454.3	14.3	PKS 1911-201	1.8
G45.07 + 00.14	SMA	3C454.3	4.6	PKS 2025+337	0.5
W51e2	SMA	Ceres	0.7	3C454.3	16.0	PKS 2025+337	0.8
NGC7538-IRS1	SMA	Ceres	0.5	3C454.3	11.9	PKS 2202+422	3.0

Note. — Flux densities derived assuming a flux density for Uranus of 36.6 Jy.

Table 2. VLA Observations

Source	RA	Dec	Line	Frequency GHz	Spectral Resolution kms ⁻¹	Band width Chan.	Angular Resolution arc second	Cont. ^a rms mJy	Date Observed
			H66 α ^b	22.36417	2.62	64	1.7 \times 1.0	9	1988-05-23
			H53 α	42.95197	1.36	64	1.5 \times 1.3	3.0	2003-02-03
G28.20 - 0.04 N	18 42 58.17	-04 13 57.0	H53 α	42.95197	1.36	64	0.6 \times 0.4	1.2	2005-06-24
			H53 α	42.95197	5.45	32	0.7 \times 0.5	3.0	2005-06-28
G45.07+0.14 N	19 13 22.069	10 50 52.5	H76 α ^c	14.69000	15.95	16	0.6 \times 0.6	10	1984-01-07
W51e2	19 23 43.913	14 30 14.7	H66 α	22.36417	2.62	64	0.3 \times 0.2	1.6	2003-02-01
			H53 α	42.95197	1.36	64	0.5 \times 0.4	0.9	2003-02-01
NGC7538-IRS1	23 13 45.37	61 28 10.4	H53 α	42.95197	5.45	31	0.2 \times 0.2	0.9	2005-04-17

^aBandwidth = channels \times spectral resolution

^bData from the VLA archives. The original observation is reported in Keto (2002a).

^cData from the VLA archives. The original observation is reported in Garay et al. (1986).

Table 3. Calibration of Centimeter Observations

Source	Band	Flux		Bandpass		Gain	
		Calibrator	Flux Jy	Calibrator	Flux Jy	Calibrator	Flux Jy
G28.20 - 0.04 N	Q	3C286	1.5	3C273	24.2	PKS 1851+005	1.9
G45.07 + 00.14 N	U	3C286	3.5	3C454.3	7.5	PKS 1923+210	2.1
W51e2	Q	3C286	1.5	3C273	10.1	PKS 1923+210	2.6
W51e2	K	3C286	2.5	3C273	19.5	PKS 1923+210	3.1
NGC7538-IRS1	Q	3C48	0.5	3C454.3	15.6	PKS 2250+558	0.8

Table 4. Recombination Line data

Source	Continuum Peak Jy/beam	Integrated Intensity Jy	Quantum Number	Line Peak mJy/beam	1σ mJy/beam	Line Velocity ^a kms ⁻¹	1σ kms ⁻¹	Line Width ^b kms ⁻¹	1σ kms ⁻¹
G10.6-0.4	0.017	3.14	92	8.1	0.2	0.6	0.5	37.5	1.2
	0.04 ^c	4.57	66	188.0	5.0	2.1	0.005	35.1	0.005
	2.1	6.0	53	219.0	4.9	2.2	0.005	31.8	0.01
	1.17	2.41	30	1040.0	28.5	3.4	0.3	24.5	0.8
G28.20-0.04 N	0.4	1.1	53	99.0	3.6	88.7	0.6	33.4	1.5
	0.56	0.72	30	930.0	22.0	92.5	0.2	20.9	0.6
G45.07+0.14	0.37	0.77	76	21.0	2.5	45.7	3.4	56.9	8.1
	0.08	0.17	30	92.0	10.2	49.4	1.8	33.2	4.2
W51e2	0.15	0.30	66	14.2	0.4	53.8	0.7	50.9	1.6
	0.17	2.3	53	42.0	1.1	59.5	0.3	32.5	1.2
	1.67	3.66	30	870.0	51.0	59.7	0.8	26.8	1.9
NGC7538-IRS1	0.2	0.7	53	23.3	1.1	-41.8	1.0	61.0	4.1
	2.56	2.79	30	4450.0	58.0	-60.5	0.4	57.3	0.8

^aLine center velocity from Gaussian fit.

^bFWHM from Gaussian fit.

^cKeto 2002

Table 5. Electron Densities from line widths

Source	Quantum Number	Line Width kms ⁻¹	1σ kms ⁻¹	n_e cm ⁻³	1σ cm ⁻³
G10.6-0.4	92	37.5	1.2	9.1×10^4	7.3×10^3
	66	35.1 ^a	0.005	7.8×10^5	3.2×10^2
	53	31.8	0.01	2.5×10^6	3.2×10^3
G28.20-0.04 N	92	74.4 ^b	2.6	2.9×10^5	1.2×10^4
	53	33.4	1.5	4.1×10^6	4.3×10^5
G45.07+0.14	76	56.9 ^d	8.1	6.1×10^5	1.8×10^5
	66	42.3 ^e	2.3	6.9×10^5	1.6×10^5
W51e2	66	50.9	1.6	1.6×10^6	9.0×10^4
	53	32.5	1.2	2.0×10^6	4.0×10^5
NGC7538-IRS1	66	180 ^c	...	1.0×10^7	...
	53	61.0	4.1	1.4×10^6	1.5×10^6

Note. — Electron density, n_e , required to produce the observed increase in the width of the cm RRL over the mm RRL by pressure broadening.

^aKeto 2002

^bSewilo et al 2004

^cGaume et al 1995a

^dGaray et al 1986. The line width measured in our analysis of this data is larger than reported in the original reference (48.1 kms⁻¹).

^eGaray et al 1985

Table 6. Integrated Intensities from Previous Observations

Source	Frequency GHz	Flux Jy	Beam Arc seconds	Reference
G10.6-0.4	23	2.4	0.1	Sollins & Ho (2005)
	22.3	4.1	0.2×0.1	Keto & Wood (2006)
	15	2.8	0.3	Ho & Haschick (1981)
	15	2.6	0.3×0.2	Turner & Matthews (1984)
	8.3	3.1	1.5×1.0	this paper
G28.20-0.04 N	5	1.7	1	Ho & Haschick (1981)
	23.7	0.98	0.3×0.2	Sollins et al. (2005b)
	15	0.54	0.5	Kurtz et al. (1994)
	8.4	0.30	0.9	Kurtz et al. (1994)
	8.3	0.30	4.9×2.7	Sewilo et al. (2004)
G45.07+0.14	345	2.71	3.0×4.0	Su et al. (2004)
	98	1.04	2.6×2.4	Hunter et al. (1997)
W51e2	147	3.7	2.0	Zhang et al. (1998)
	88.2	1.23	6×5	Rudolph et al. (1990)
	23.7	0.35	5×4	Rudolph et al. (1990)
	14.7	0.26	4.1×3.9	Garay et al. (1985)
	8.3	0.07	2.4	Mehring (1994)
	5.0	≤ 0.03	4.1	Mehring (1994)
	5.0	0.025	0.5	Rudolph et al. (1990)

Table 7. Model HII regions for continuum SEDs

Source	Distance kpc	Constant Density		Density Gradient		
		radius pc	density cm^{-3}	radius pc	density cm^{-3}	exponent
G010.6 - 0.4	6.0	0.05	6.0×10^4	0.05	3.5×10^4	-1.4
G28.20 - 0.04 N	9.1	0.03	9.0×10^4	0.043	1.0×10^4	-2.5
G045.07 + 00.14	9.7	0.025	1.6×10^5	0.05	1.5×10^4	-1.7
W51e2 ^a	7.0	0.01	3.0×10^5	0.01	1.0×10^5	-2.5
NGC7538-IRS1 ^b	3.5	0.02	2.7×10^6	0.08	2.7×10^6	-2.0
NGC7538-IRS1 ^c	...	0.08	5.0×10^4

^aSED also includes a contribution from dust modeled as $4500 M_{\odot}$ of cold, dusty gas with a temperature of 100 K and a dust emissivity, $\beta = 1.5$ from the model of Rudolph et al. (1990).

^bConstant density model with 3 components, 2 HII regions plus dust from the model of Pratap et al. (1992). The first HII component SED also includes a contribution from dust modeled as $53 M_{\odot}$ of cold, dusty gas with a temperature of 50 K and a dust emissivity, $\beta = 1.0$

^cSecond component of constant density model.

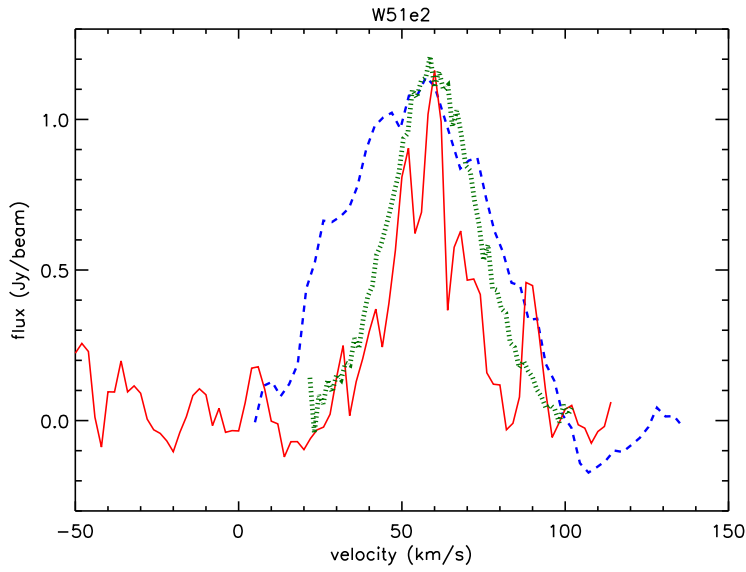


Fig. 1.— H66 α (dashed blue line), H53 α (dotted green line), and H30 α (solid red line) in W51e2. The flux densities of the H66 α line and the H53 α lines have been multiplied by 80 and 27, respectively.

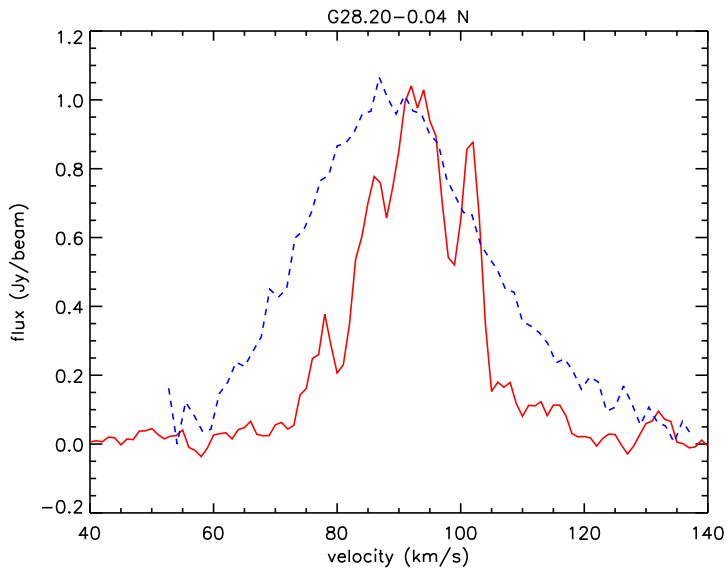


Fig. 2.— H53 α (dashed blue line) and H30 α (solid red line) in G28.20-0.04N. The flux density of the H53 α line has been multiplied by 10.

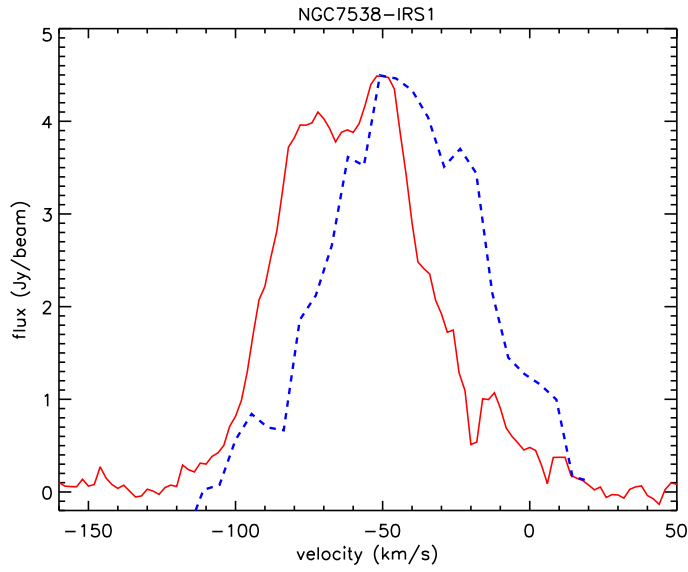


Fig. 3.— H30 α (solid red line) and H66 α (dashed blue line) in NGC7538-IRS1. The flux density of the H66 α has been multiplied by 190.

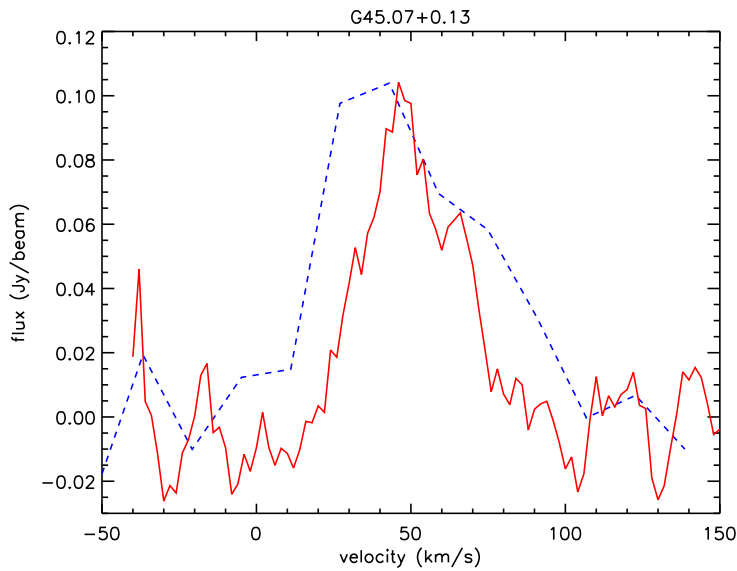


Fig. 4.— H76 α (dashed blue line) and H30 α (solid red line) in G45.07+0.13. The flux density of the H76 α line has been multiplied by 5.

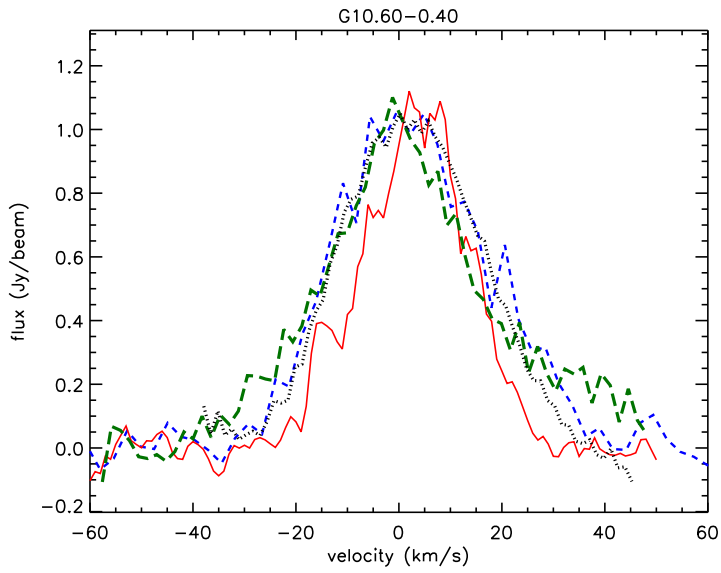


Fig. 5.— $H2\alpha$ (long-dashed green line), $H66\alpha$ (short-dashed blue line), $H53\alpha$ (dotted black line), and $H30\alpha$ (solid red line) in G10.6-0.04. The flux densities of the $H2\alpha$, $H66\alpha$, and $H53\alpha$ lines have been multiplied by 115, 5.5, and 4.8 respectively.

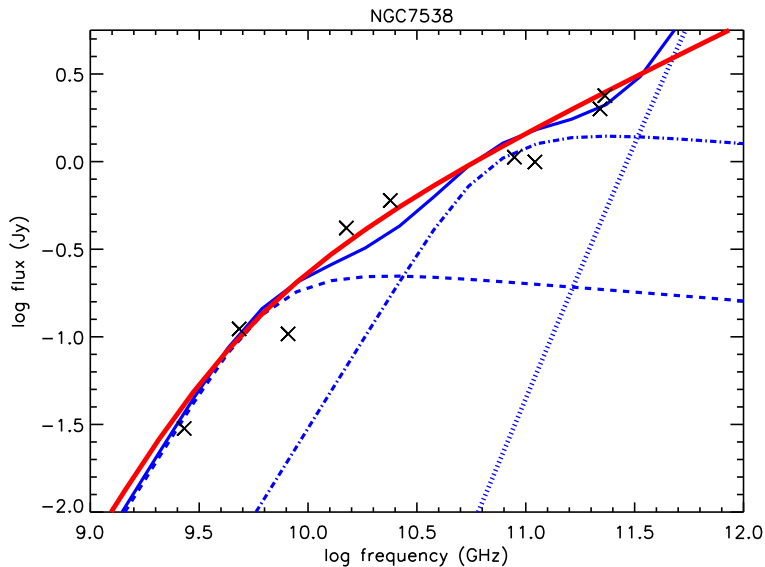


Fig. 6.— SED NGC 7538 IRS1. Data are from table 1 of Pratap et al. (1992) with the addition of our 230 GHz SMA observation. The blue lines show a 3 component model proposed by Pratap et al. (1992) consisting of two HII regions plus dust (dotted line). The dash-dotted line (of the smaller, higher density component) is shifted upward and to the right of the dashed line (of the larger, lower density component). The wavy solid blue line shows the sum of the three components. The red solid line that crosses smoothly through the waves of the three component model shows the SED of a single HII region with a power-law density gradient. See §3 and table 7.

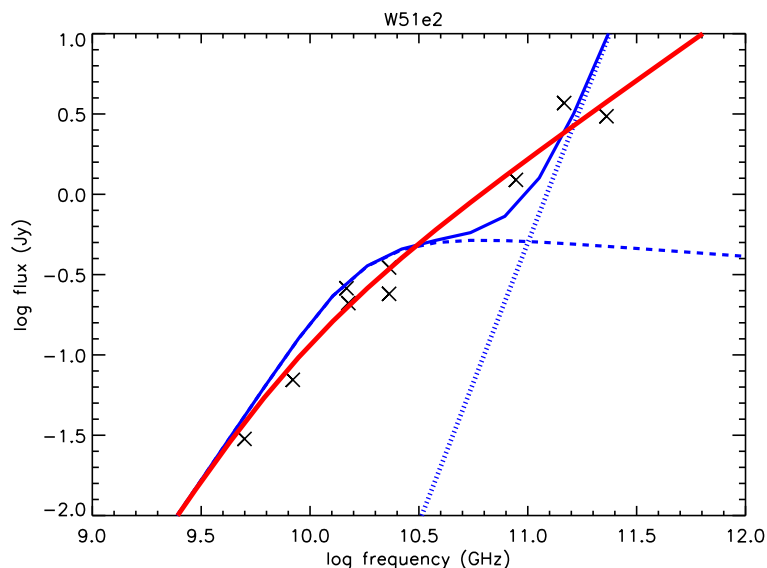


Fig. 7.— Measured flux densities of the W51e2 HII region (crosses). The blue dashed lines show a two-component model proposed by Rudolph et al. (1990) consisting of a uniform density HII region plus dust (dotted line). The solid red line is the SED predicted for an HII region with a density gradient ($n_e \propto r^{-1.5}$) and no significant dust emission. See §3 and table 7.

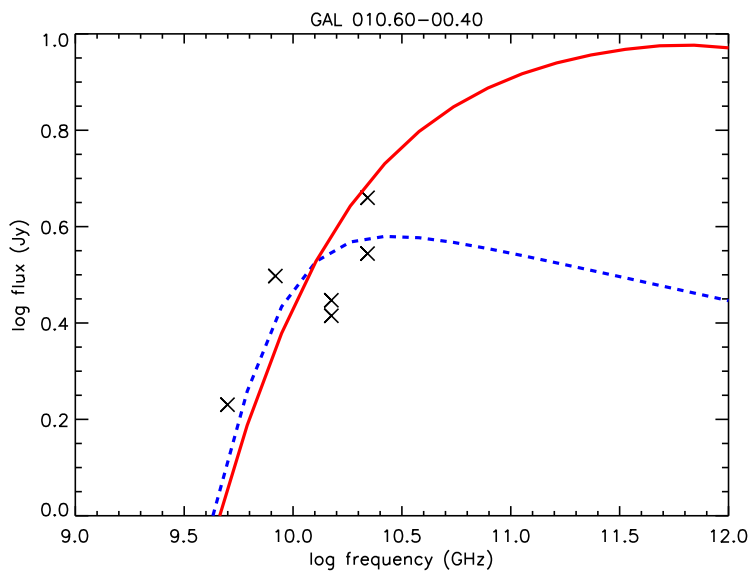


Fig. 8.— Measured flux densities of the G10.6-0.4 HII region (crosses). The blue dashed line is a model based on a uniform density HII region; the red line is a model based on an HII region with a density gradient.

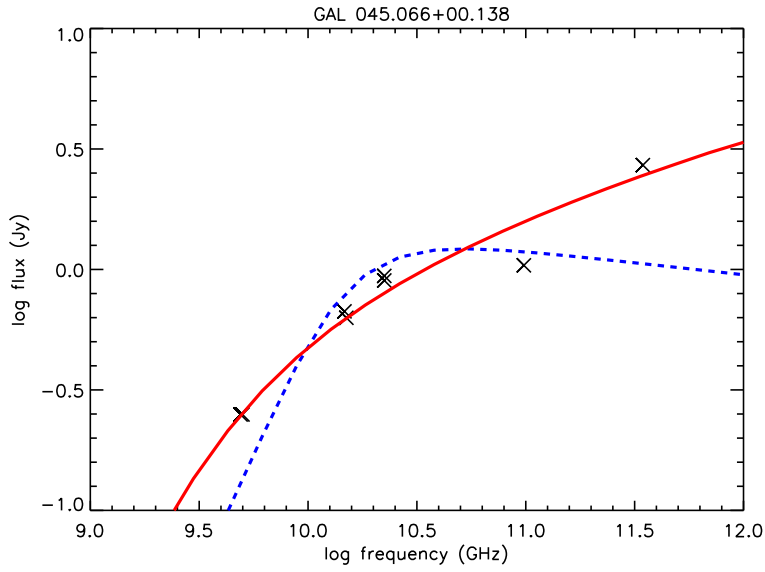


Fig. 9.— Continuum spectral energy distribution for G45.07+00.14. The crosses mark the observations; the blue dashed line is a model based on a uniform density HII region; the red line is a model based on an HII region with a density gradient.

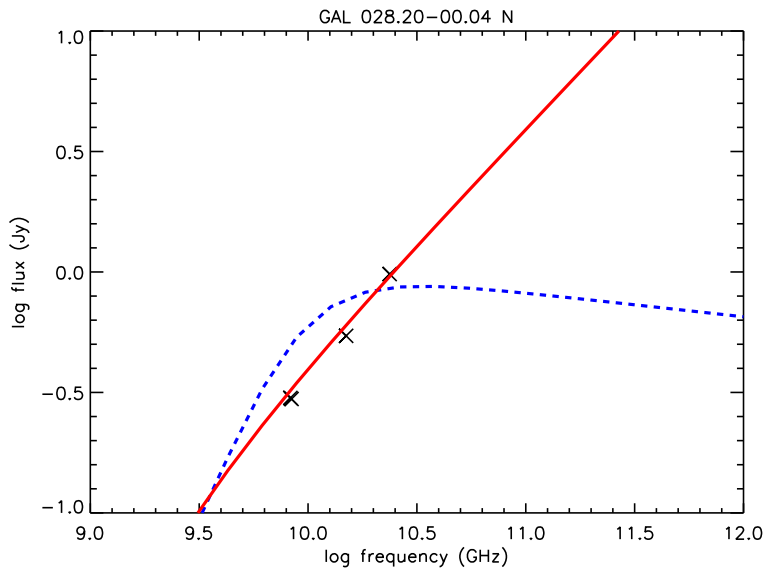


Fig. 10.— Continuum spectral energy distribution for G28.20-0.04. The crosses mark the observations; the blue dashed line is a model based on a uniform density HII region; the red line is a model based on an HII region with a density gradient.